Time-Dependent Raman Analysis of Metal-to-Ligand Charge Transfer Excited States: Application to Radiative and NonRadiative Decay

Darla Graff Thompson,[†] Jon R. Schoonover,[‡] Cliff J. Timpson,[||] and Thomas J. Meyer*,[§]

University of North Carolina at Chapel Hill, Chapel Hill, North Carolina 27599, and
Los Alamos National Laboratory, Los Alamos, New Mexico 87544

Received: March 18, 2003; In Final Form: July 11, 2003

The photophysical properties of the emitting metal-to-ligand charge transfer (MLCT) excited states of the complexes, $[Os(bpy)_3]^{2+}$, $[Os(bpy)_2(py)_2]^{2+}$, and $[Os(bpy)(py)_4]^{2+}$ (bpy = 4-4′-bipyridine, py = pyridine) have been characterized in aqueous solution at room temperature by absorption, emission, and Raman spectroscopies and by emission lifetimes and emission quantum yields. A spectroscopic model has been developed by using the time-dependent theory of Raman scattering, taking into account interference effects on resonance Raman profiles arising from interactions between the different ligands. A model based on the cylindrical model of Sension and Strauss provides a good fit to the data. The mode-specific vibrational parameters obtained from the spectroscopic analysis are used to calculate the vibrational contributions to the radiative and nonradiative decay rate constants for each of the complexes. These results and the experimental rate constants were used to calculate vibrationally induced electronic coupling matrix elements (V_k) for nonradiative decay and also transition moments, M, for radiative decay. For radiative decay, the average transition moment for the three complexes was 0.05Å, and for nonradiative decay, the average value of V_k was 910 cm^{-1}. Within a reasonable margin of error, the Franck−Condon contributions are in agreement with values obtained in a previous study that used the single mode approximation and a Franck−Condon analysis of emission spectra.

Introduction

Time-dependent interpretations of resonance Raman data have been successfully applied to a variety of molecules.[1−12] The $\delta-\delta^*$ electronic transitions in the multiply metal−metal bonded molecules $M_2X_8^{-2}$ (X = F, Cl, Br, or I; M = Re or Mo) exhibit intense Raman overtones, allowing detailed structural information to be obtained.[2,13] UV resonance Raman scattering has been used to probe and model the dissociative mode of excited alkyl-iodide molecules.[3] The equilibrium displacements of vibrational modes coupled to charge-transfer in organic donor−acceptor molecules have been determined,[4] and this information has been used in calculating electron-transfer rate constants.[5] Vibrational coupling to intervalence transfer in mixed-valence complexes has been analyzed by using near-IR excitation and relationships from time-dependent Heller theory.[6−8,14−16] Many biological systems have been analyzed,[9−12] including a mode-specific study of the vibrations and torsional deformations in the retinal chromophore of rhodopsin upon resonant excitation with visible light.[9]

While it has been well established[17−24] that the Franck−Condon factors that help dictate rate constants for electronic processes are also responsible for spectral band shapes (absorption, emission, and Raman) of analogous electronic transitions, most of the experimental demonstrations have been based on absorption and emission spectra.[22,25−28] Resonance Raman profiles provide explicit vibrational information for each coupled mode and a quantitative description of the Franck−Condon factors, but there are few examples in the literature where this information has been related to kinetic parameters.[4−6,8,16]

The goal of the current study was to model absorption, emission, and resonance Raman profiles for the metal-to-ligand-charge-transfer (MLCT) transitions of a series of Os-2,2′-bipyridine complexes and to use the resulting spectral parameters to calculate rate constants for radiative and nonradiative decay in the associated MLCT excited states.

A complete vibrational study of the series $[Os(bpy)(py)_4]^{2+}$, $[Os(bpy)_2(py)_2]^{2+}$, and $[Os(bpy)_3]^{2+}$ (bpy = 2,2′-bipyridine, py = pyridine) was of particular interest. These molecules are a subset of a series of nearly 30 complexes of the type $[Os(bpy,phen)L_4]^{n+}$ (phen = 1,10 phenanthroline and L = halides, nitrogen donors, phosphines, CO). They have been used in previous studies[22,23,29−31] to probe relationships between the Energy Gap Law for nonradiative decay and kinetic parameters derived from Franck−Condon analyses of emission spectra. We were interested in comparing the earlier results with those derived from a complete vibrational analysis based on resonance Raman profiles. We also wanted to apply the results of the mode-for-mode analysis to the dynamics of radiative and nonradiative decay based on the Einstein equation for spontaneous emission and the Energy Gap Law.

Transition metal-polypyridine complexes have been fundamental in the design of molecular assemblies for the study of photoinduced energy- and electron-transfer.[32,33] Understanding and demonstrating the theoretical relationships between spectral and kinetic properties of the chromophores that are at the heart of these assemblies remains an important endeavor.

---

* To whom correspondence should be addressed. E-mail: tjmeyer@lanl.gov.

[†] Current address: DX-2, MS C920, Los Alamos National Laboratory, Los Alamos NM 87544.

[‡] Current address: MST-7, MS E549, Los Alamos National Laboratory, Los Alamos NM 87544.

[§] Current address: ADSR, MS A127; Los Alamos National Laboratory, Los Alamos NM 87544.

[||] Department of Chemistry, Roger Williams University, Bristol RI 02809.

10.1021/jp0303366 CCC: $25.00

Experimental Methods

Materials. Deionized, nano-pure water was used as the solvent in all spectroscopic measurements. Na_2SO_4, used as a reference in the resonance Raman experiments, was purchased from Aldrich and used without further purification. The salts $[Os(bpy)_3]Cl_2$ and $[Os(bpy)_2(py)_2]Cl_2$ were available from previous studies,[22,23] and $[Os(bpy)(py)_4]Cl_2$ was synthesized by a published procedure.[34]

Measurements. UV−vis absorption spectra were measured on a CARY 14 spectrophotometer with an Olis upgrade. The pure solvent background was subtracted from sample spectra by using the procedure provided by the manufacturer.

Resonance Raman spectra were obtained following continuous wave excitation from Ar^+ (Spectra Physics 164) or Kr^+ (Coherent Innova 90) lasers. The incident beam was focused onto a spinning cell containing approximately 2 mL of solution. Raman scattering was collected with a backscattering geometry, the detection angle being 135° relative to the incident laser beam, to minimize self-absorption. The scattered light was collected and passed through a polarization scrambler into a Jobin Yvon U1000 double monochromator with an 1800 g/mm ruled grating. The entrance and exit slits were adjusted with each line of excitation to maintain a resolution of 4 cm^{-1}. The signal was detected with an RCA 31034-C PMT, and collected with the Enhanced Prism software package from Instruments, S. A., Jobin Yvon.

Emission profiles and quantum yields were measured on a Spex Fluorolog 212 photon counting fluorimeter. The spectra were corrected for instrument response with the procedure provided by the manufacturer. Absorbance values at the excitation wavelength were ∼0.1. The samples were bubble deaerated with argon gas for 15 min.

Emission lifetime measurements were conducted by using a PRA LN 1000/LN 102 nitrogen laser/dye laser combination for sample excitation. Emission was monitored at a right angle to the excitation by using a PRA B204−3 monochromator and a cooled, 10-stage Hamamatsu R928 PMT coupled to a LeCroy 7200A digital oscilloscope interfaced to an IBM PC. Solutions were the same as those prepared for the emission quantum yield measurements. Transient signals were measured near the emission maxima (740 nm for $[Os(bpy)_3]Cl_2$, 780 nm for $[Os(bpy)_2(py)_2]Cl_2$, and 790 nm for $[Os(bpy)(py)_4]Cl_2$).

Programs used in the spectral fitting procedure were written in Microsoft Fortran 5.0 and run on a 66 MHz 486 computer.

Correction Factors and Internal Standards. Correction for detector response was made by using a 200 W quartz-halogen tungsten lamp operated at 65 Amps dc (Optronics Laboratories standard of spectral irradiance (OL220M) M-774). The measured spectra were multiplied by $L(\lambda)/I(\lambda)$, where $L(\lambda)$ is the spectrum of the lamp output, and $I(\lambda)$ is the spectrum of the lamp measured by the detector. The magnitude of this correction was negligible.

Integration of the individual Raman vibronic peak areas was performed by using a linear baseline. The *relative* Raman cross-sections for each j mode, σ'_j, were calculated relative to the Raman cross-section of the 982 cm^{-1} sulfate peak, σ'_*, which was arbitrarily set equal to 1. Correction for self-absorption was performed in accordance with the method of Myers et al.[4,35,36]

The per-molecule differential cross-section of the jth vibration, σ'_j, relative to the standard ($\sigma'_* = 982$ cm^{-1} band of $SO_4{}^{-2}$)[37,38] is given by eq 1

$$\sigma'_j = \frac{[C_*]}{[C_j]}\sigma'_* \tag{1}$$

In eq 1, C_* is the concentration of sulfate ion in solution (0.5 M), and C_j is the sample concentration.

The differential Raman cross-sections calculated from the experimental Raman intensities are related to the total Raman cross-section, σ_{total}, by the equation

$$\sigma_{\mathrm{total}} = \frac{8\pi}{3}\cdot\frac{(1+2\rho)}{(1+\rho)}\left(\frac{\partial\sigma}{\partial\Omega}\right)_{||+\perp} \tag{2}$$

where ρ is the depolarization ratio. We made polarized measurements at two wavelengths and found ρ values around 0.4, consistent with the values reported by Miller et al.,[39] for the ^{1}MLCT resonance-enhanced modes of $Fe(bpy)_3{}^{2+}$, $Fe(bpy)(CN)_2$, and $Fe(bpy)(CN)_4{}^{2-}$. A value of $\rho = 0.4$ was used in our calculations to relate equations for σ_{total} and $(\partial\sigma/\partial\Omega)_{||+\perp}$.

Time-Dependent Theory. In the time-dependent formalism,[40−45] the differential Raman cross-section of the Rth normal mode is related to the Raman polarizability, α'_R, by

$$\left(\frac{d\sigma_R}{d\Omega}\right)_{||+\perp} = \frac{4E_S^3E_L}{15\hbar^4c^4}\int_{-\infty}^{\infty} G(\beta)|\alpha'_R|^2\cdot d\beta \tag{3}$$

where

$$\alpha'_R = \frac{e'^2M^2}{\hbar}\int_0^{\infty}\exp\left[\frac{i(E_L - E_{00})t}{\hbar} - \frac{i\beta t}{\hbar} - g(t)\right]S_R \times (\exp^{(-i\omega_R t-1)})\prod_{j=1}^{N}\exp(-S_j[1 - e^{(-i\omega_j t)}])dt \tag{4}$$

The prime notation indicates that the inhomogeneous broadening term, β (see below), is included. In eqs 3 and 4, E_L is the laser energy, E_S is the scattering energy ($E_L - \hbar\omega_R$), $\hbar\omega$ is the vibrational quantum spacing, and R is the normal coordinate. The dimensionless electron-vibrational coupling constant, S, is related to the change in equilibrium displacement between states, ΔQ_{eq}, by $S = (\mu\omega/\hbar)(\Delta Q_{eq})^2$, where μ is the reduced mass. M is the transition dipole (in Å), and E_{0-0} is the 0−0 transition energy between the ground and excited states. $G(\beta)$, the inhomogeneous broadening term, is defined in eq 5, with σ being the standard deviation.

$$G(\beta) = \frac{1}{\sigma\,(2\pi^{1/2})}\exp\left(\frac{-\beta^2}{2\sigma^2}\right) \tag{5}$$

Homogeneous broadening is included in the complex function $g(t)$.[46,47] In the "slow modulation" limit, with strong electron−solvent coupling, $g(t)$ gives rise to a Gaussian distribution having full-width at half-maximum (fwhm) = $(8 \ln 2)^{1/2}\,\Gamma$ and a $\Gamma^2/2kT$ Stokes shift in the energy of the spectral distribution, eq 6

$$g(t) = \frac{\Gamma^2t^2}{2\hbar^2} + i\,\frac{\Gamma^2 t}{\hbar\,2kT} \tag{6}$$

The absorption cross-section for the transition responsible for resonance enhancement is given by eq 7

$$\sigma_A = \frac{4\pi E_L e^2M^2}{6\hbar^2cn}\int_{-\infty}^{\infty}G(\beta)\int_{-\infty}^{\infty}\times \exp\left[\frac{i(E_L - E_{00})t}{\hbar} - \frac{i\beta t}{\hbar} - g(t)\right]\prod_{j=1}^{N}\exp(-S_j[1 - e^{(-i\omega_j t)}])dt\,d\beta \tag{7}$$

and can be related to the molar absorptivity ($M^{-1}cm^{-1}$) by

$$\epsilon_{abs} = 4.342 \times 10^{-19}\sigma_A N_A \qquad (8)$$

where N_A is Avogadro's number.

Transform theory has been used to derive expressions for fluorescence rate constants,[46] quantum yields,[48] and cross sections.[49−51] An alternate approach makes use of the vibrational overlap part of the Heller theory expression,[52] see eq 7 for absorption, with the appropriate E_s^3 prefactor, to fit the emission band shape

$$I_{em}(E_S) = E_S^3 F(E_S) = \frac{E_S^3}{2\pi}\int_{-\infty}^{\infty} G(\beta)\int_{-\infty}^{\infty} \exp\left[\frac{i(E_{00}-E_S)t}{\hbar} - g(t)\right]\prod_{j=1}^{N} \times \exp(-S_j[1-e^{(-i\omega_j t)}])\,dt\,d\beta \qquad (9)$$

In eq 9, I_{em} is the emission intensity with the calculated spectrum normalized so that the maximum coincides with the measured profile.

The radiative rate constant, k_r, in photons per second is given by

$$k_r = \frac{2nM^2}{3\pi\hbar^5 c^3}\int_{-\infty}^{\infty} E_s^3 F(E_s)\,dE_s \qquad (10)$$

where the integrand is the expression given in eq 9 and M is the transition moment between the emitting state and ground state.

The nonradiative rate constant is given by[46]

$$k_{nr} = \frac{2|V_k|^2}{\hbar}\int_{-\infty}^{\infty} G(\beta)\int_{0}^{\infty} \exp\left[\frac{i(E_{00})t}{\hbar} - \frac{i\beta t}{\hbar} - g(t)\right]\prod_{j=1}^{N} \times \exp(-S_j[1-e^{(-i\omega_j t)}])\,dt\,d\beta \qquad (11)$$

V_k is the vibrationally induced electronic coupling matrix element for nonradiative decay.[19,20]

Interference Effects. With multiple contributing states, the molecular polarizability tensor is given by eq 12[53−55]

$$\vec{\alpha} = \begin{bmatrix} \alpha_{xx} & \alpha_{xy} & \alpha_{xz} \\ \alpha_{yx} & \alpha_{yy} & \alpha_{yz} \\ \alpha_{zx} & \alpha_{zy} & \alpha_{zz} \end{bmatrix} \qquad (12)$$

In fluid solution, the tensor components are separately unobservable due to free rotation. The three Cartesian elements give rise to Placzek or "rotational" invariants, which are experimentally discernible.[53] They are given by

$$\Sigma^0 = \frac{1}{3}|\alpha_{xx} + \alpha_{yy} + \alpha_{zz}|^2 \qquad (13a)$$

$$\Sigma^1 = \frac{1}{2}[|\alpha_{xy} - \alpha_{yx}| + |\alpha_{xz} - \alpha_{zx}|^2 + |\alpha_{yz} - \alpha_{zy}|^2] \qquad (13b)$$

$$\Sigma^2 = \frac{1}{2}[|\alpha_{xy} + \alpha_{yx}| + |\alpha_{xz} + \alpha_{zx}|^2 + |\alpha_{yz} + \alpha_{zy}|^2] + \frac{1}{3}[|\alpha_{xx} - \alpha_{yy}|^2 + |\alpha_{xx} - \alpha_{zz}|^2 + |\alpha_{yy} - \alpha_{zz}|^2] \qquad (13c)$$

with, Σ°, the isotropic (symmetric) part of the tensor; Σ^1, the antisymmetric part, and Σ^2, the symmetric anisotropy. The total differential Raman cross-section is given by

$$\left(\frac{d\sigma}{d\Omega}\right)_{\|+\perp} = \sum_{\lambda,\lambda'}|\alpha_{\lambda,\lambda'}|^2 = \frac{4E_S^3 E_L e'^2}{15\hbar^4 c^4}\left(\frac{1}{8}(10\Sigma^0 + 5\Sigma^1 + 7\Sigma^2)\right) \qquad (14)$$

where $e' = e/(4\pi\epsilon_o)^{1/2}$ is the electron charge in a vacuum.

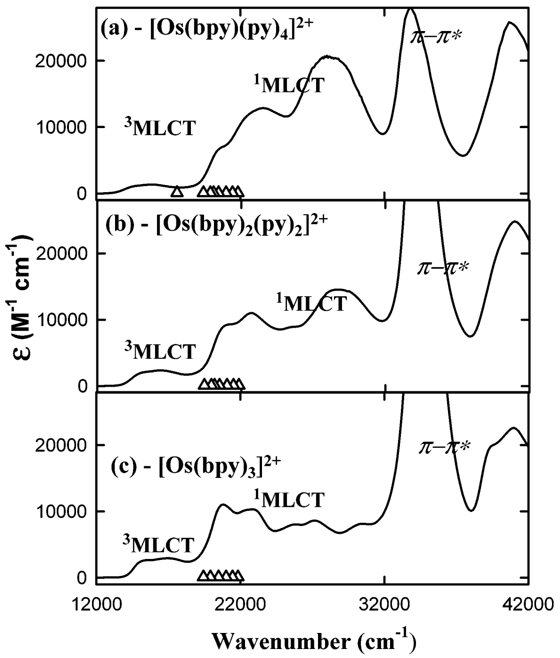

Figure 1. UV−vis absorption spectra (240−833 nm) for $[Os(bpy)(py)_4]^{2+}$, $[Os(bpy)_2(py)_2]^{2+}$, and $[Os(bpy)_3]^{2+}$ in water. Spectral regions for ^{3}MLCT, ^{1}MLCT, and $\pi-\pi^*$ absorptions are indicated. Triangles indicate the argon and krypton laser lines used for Raman excitation.

Results

In Figure 1, are shown absorption spectra of the three complexes (solid lines). Bands on the high-energy side (> 32 000 cm^{-1}) arise from py- and bpy-localized $\pi \rightarrow \pi^*$ transitions. Largely singlet metal-to-ligand-charge-transfer (^{1}MLCT) transitions to both types of ligands occur from 19 000 to 32 000 cm^{-1} and the analogous, weakly allowed, largely triplet ^{3}MLCT transitions from 14 000 to 19 000 cm^{-1}.[40,56,57] Spin−orbit coupling at Os ($\xi(Os^{II}) \sim 3000$ cm^{-1}) strongly mixes the spin character of the states.

The argon and krypton laser excitation frequencies for resonance Raman scattering are shown in Figure 1. Attempts were made to acquire spectra at 647 and 676 nm by direct ^{3}MLCT enhancement, but this was not possible with our system because of competing emission.

The separate MLCT bpy and py contributions were deconvoluted as follows (see Figure 1S): The bpy contribution to $[Os(bpy)(py)_4]^{2+}$ in Figure 1Sa was estimated as one-third of the $[Os(bpy)_3]^{2+}$ spectrum in Figure 1Sc, and the py contribution was estimated by subtracting one-third of the $[Os(bpy)_3]^{2+}$ spectrum from $[Os(bpy)(py)_4]^{2+}$. Agreement between half of the pyridine contribution for $[Os(bpy)(py)_4]^{2+}$ with the py contribution for $[Os(bpy)_2(py)_2]^{2+}$ was very good, showing an internal consistency in the subtraction process and supporting the coarse approximation of independent ^{1}MLCT transitions for absorption.

Typical examples of resonance Raman data with excitation at 476.5 nm are shown in Figure 2S. In Figure 2 are shown

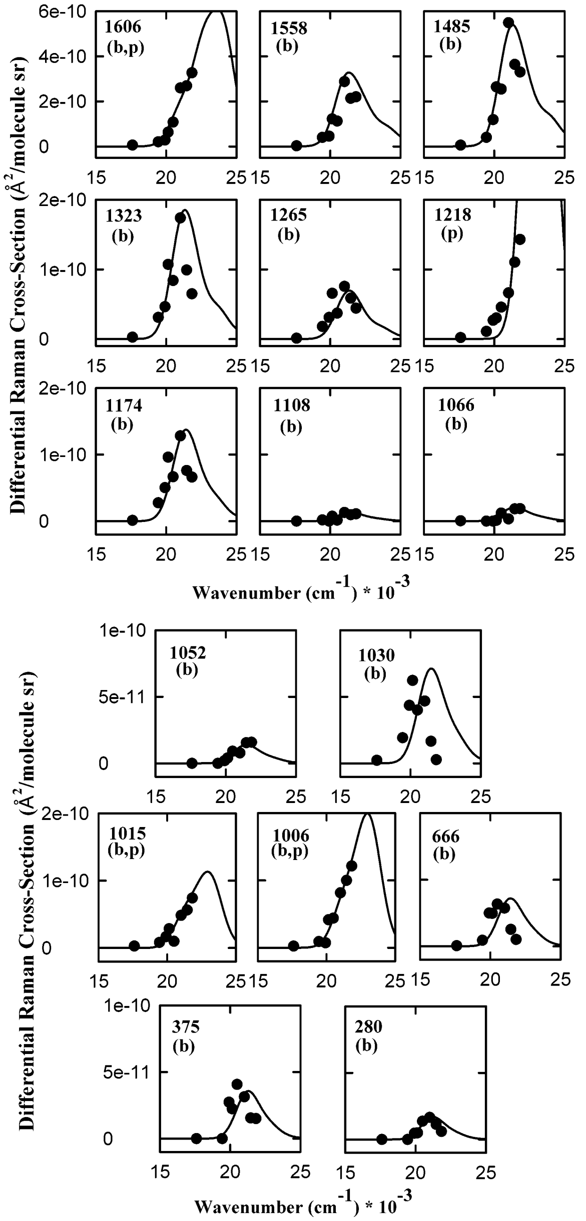

Figure 2. Calculated and experimental resonance Raman excitation profiles for $[Os(bpy)(py)_4]^{2+}$ in H_2O at ambient temperature. Parameters used in the calculations are listed in Table 1.

Raman excitation profiles in units of differential cross-section, Å^2 molecule^{-1} sr^{-1}, for $[Os(bpy)(py)_4]^{2+}$. Profiles for $[Os(bpy)_2(py)_2]^{2+}$ and $[Os(bpy)_3]^{2+}$ are available in Figures 3S and 4S. Cross-section values are listed in Table 1.

Corrected emission spectra in water at 25 °C are shown in Figure 3. Excited-state lifetimes (±20%) by exponential fitting of transient emission decays at peak maxima were $[Os(bpy)_3]^{2+}$, 20 ns; $[Os(bpy)_2(py)_2]^{2+}$, 14 ns; $[Os(bpy)(py)_4]^{2+}$, 10 ns. Emission quantum yields (ϕ_{em}) were calculated by using eq 16 with $Os(bpy)_3{}^{2+}$ in CH_3CN as the reference (ϕ_*), and

$$\phi_{em} = (\phi_*)\,\frac{\text{Abs}}{\text{Abs}_*}\left(\frac{\eta}{\eta_*}\right)^2\frac{\text{IntA}}{\text{IntA}_*} \tag{15}$$

Abs is the sample absorbance at the excitation wavelength, η is the solvent refractive index, and IntA is the integrated area of the emission. Quantum yields for the three complexes are listed in Table 2 as are radiative (k_r) and nonradiative (k_{nr}) rate constants, calculated from ϕ and τ by using the expressions

$$k_r = \frac{\phi_{em}}{\tau} \tag{16a}$$

$$k_{nr} = \frac{1}{\tau} - k_r \tag{16b}$$

TABLE 1: Differential Cross-Sections[a] Calculated from Resonance Raman Excitation Profiles in Water at 23 °C

(a) $Os(bpy)(py)_4{}^{2+}$

Raman band energy (cm^{-1})	excitation wavelength (nm) 458	466	476	488	496.5	502	514.5	568
1606	32.7	26.9	25.9	10.8	6.3	2.9	2.0	0.6
1558	22.0	21.3	28.8	11.3	12.2	4.6	4.0	0.3
1485	33.0	36.4	54.9	25.5	26.4	11.9	4.0	0.6
1323	6.5	9.9	17.4	8.4	10.7	4.7	3.1	0.3
1265	4.4	5.9	7.6	3.7	6.6	3.1	1.8	0.1
1218	14.3	11.0	6.6	4.6	3.0	2.7	1.1	0.2
1174	6.6	7.6	12.8	6.7	9.6	5.0	2.8	0.1
1108	1.1	1.0	1.3	0.1	0.7	0	0.2	0
1066	1.9	1.9	0.3	1.2	0.1	0	0	0.1
1053	1.6	1.6	0.8	0.9	0.4	0.2	0	0
1030	0.3	1.7	4.7	4.0	6.2	4.4	1.9	0.2
1015	7.4	5.7	4.9	1.0	2.9	1.7	0.8	0.3
1006	12.2	10.0	8.2	4.4	4.2	0.7	0.9	0.2
666	1.0	2.5	5.7	6.3	5.0	5.0	0.9	0.1
375	1.5	1.6	3.1	4.1	2.2	2.7	0	0
280	0.6	1.1	1.7	1.4	0.5	0.5	0	0

(b) $Os(bpy)_2(py)_2{}^{2+}$

Raman band energy (cm^{-1})	excitation wavelength (nm) 458	466	476	488	496.5	502	514.5
1606	21.0	16.4	14.4	6.8	3.9	1.48	1.1
1558	28.1	25.0	27.1	11.7	9.6	3.62	3.5
1485	48.4	53.9	57.1	25.7	26.1	10.9	8.0
1323	11.3	16.1	18.0	9.1	9.6	4.0	3.2
1265	6.4	10.1	9.9	4.1	5.2	2.7	1.8
1218	2.4	0.8	0.5	0.4	0	0	0
1174	10.6	17.1	14.7	6.7	7.8	4.5	2.9
1108	0		0.2	0.3	0.3	0.4	0
1066	0.6		0.3	0.3	0.1	0	0
1036	0.2		2.5	1.6	2.1	2.0	0.9
1026	2.5		5.1	2.6	3.1	1.9	0.5
1012	7.1	4.8	5.6	1.5	2.5	0.9	0
670	2.3	2.5	7.63	6.4	4.6	3.6	0.7
375	1.3		3.6	4.7	0.3	1.3	0
288	0.5		0.6	1.0	0.7	0	0

(c) $Os(bpy)_3{}^{2+}$

Raman band energy (cm^{-1})	excitation wavelength (nm) 458	466	476	488	502	514.5
1606	17.6	16.7	13.2	5.7	1.1	0.8
1558	33.8	34.1	33.3	13.3	5.6	3.4
1485	70.0	79.4	80.9	35.1	19.6	11.4
1323	19.5	23.3	26.5	12.7	8.7	5.1
1265	13.1	16.8	17.8	7.0	8.1	5.1
1174	16.2	23.9	20.7	9.8	7.9	4.9
1108	1.0	0.4	0.2	0.5	0	0
1046	0.3	1.0	1.6	1.5	0.4	1.3
1027	7.4	9.0	12.8	6.0	2.3	2.0
1015	3.6	4.6	3.37	2.1	0	0
673	2.4	6.3	9.8	9.0	4.4	0.7
374	1.9	2.9	3.6	4.6	0	0.4

[a] Differential cross-sections in units of Å^2 molecule^{-1} sr^{-1} × 10^{11}.

Two-State Model and Multi-Mode Analysis. *General Considerations.* The resonantly enhanced bpy modes of A_1 symmetry at 1606, 1558, 1485, 1323, 1265, 1174, 1066, 1053, 1030, 1115, 1006, 666, 375, and 280 cm^{-1} can be assigned based

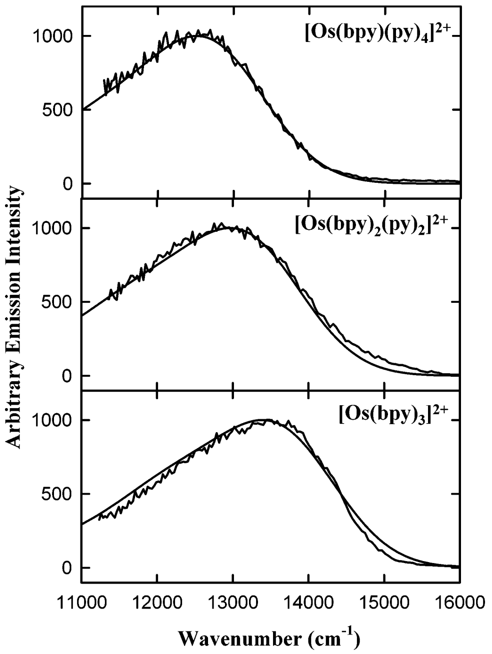

Figure 3. Corrected emission spectra in water at ambient temperature. Also shown are normalized spectral profiles calculated by using the multi-mode results from the two-state modeling of absorption and Raman profiles and the bpy parameters from Table 3. The E_0 values in the fits were 12 500 cm^{-1} for [Os(bpy)(py)$_4$]$^{2+}$, 13 000 cm^{-1} for [Os(bpy)$_2$(py)$_2$]$^{2+}$, and 13 500 cm^{-1} for [Os(bpy)$_3$]$^{2+}$; constant multipliers for S_j values were 0.87, 1.2, and 1.5; $\Delta\bar{\nu}_{1/2} = 1907$ cm^{-1}; standard deviation $\sigma = 810$ cm^{-1}. See text for details.

TABLE 2: Photophysical Parameters in Water at 23 °C (Estimated Error in Parentheses)

	Os(bpy)(py)$_4$$^{2+*}$	Os(bpy)$_2$(py)$_2$$^{2+*}$	Os(bpy)$_3$$^{2+*}$
$\lambda_{\mathrm{max,em}}$(nm)	790	780	740
Φ_{em}	0.0007	0.0004	0.0003
$^{a}k_{\mathrm{r}}$, s^{-1}	4×10^4	3×10^4	3×10^4
$^{a}k_{\mathrm{nr}}$, s^{-1}	5.0×10^7	7.4×10^7	1.0×10^8

[a] Uncertainties in these values are on the order of ±20%.

on the normal coordinate analysis by Kincaid et al.[58,59] for [Ru(bpy)$_3$]$^{2+}$. Raman spectra and assignments for [Os(bpy)$_3$]$^{2+}$ have also been reported by Bradley et al.[60] Pyridine modes were assigned based on resonance Raman studies on metal-to-pyridine charge-transfer transitions.[61,62] The only exclusively enhanced py band appears at 1218 cm^{-1}. The others are indistinguishable from bpy bands at or near the same frequency and appear at 1606, 1015, and 1006 cm^{-1}. There are some slight differences in the normal-mode frequencies between the three complexes in the 1000 to 1053 cm^{-1} region as found earlier in the series [Os(bpy)$_3$]$^{2+}$, [Os(bpy)$_2$(P$_2$)]$^{2+}$, and [Os(bpy)(P$_2$)$_2$]$^{2+}$, where P$_2$ = *cis*-Ph$_2$PHC=CHPPh$_2$.[63]

Absorption spectra are dominated by ^{1}MLCT transitions that are py-based (~23 000 and ~28 000 cm^{-1}) and bpy-based (~20 000 cm^{-1}). In the Raman excitation profiles, ~17 600 to ~21 800 cm^{-1}, bpy enhancement dominates with pre-resonant contributions from the higher-lying py transition(s). The intensity profile of the band at 1485 cm^{-1} rises, passes through a maximum, and falls, as expected for single state enhancement. By contrast, the 1218 cm^{-1} py band intensity continues to rise to higher energy with no maximum, consistent with pre-resonant enhancement. Raman profiles for modes common to both ligands at 1606, 1015, and 1006 cm^{-1} pass through apparent local maxima in the bpy region and increase in intensity at higher energy.

Raman Spectral Analysis and the Os(L)$_6$ Polarizability Model. In the spectral region for Raman enhancement in [Os(bpy)$_3$]$^{2+}$ (17 600 to 21 800 cm^{-1}), there are four ^{1}MLCT bands separated[56,57,64,65] by ~700, 2100, and 2900 cm^{-1} (8 K). The lowest, most intense singlet MLCT transition is x−y-polarized with weaker, z-polarized transitions also contributing. To simplify the analysis, it was assumed that both the bpy and py MLCT contributions could be represented as arising from single bpy and py MLCT excited states. While this is clearly an oversimplification, the various transitions do have the same d$\pi^6 \rightarrow$ d$\pi^5\pi^{*1}$ orbital parentage.

The results of the absorption spectral deconvolution showed that, to a first approximation, bpy and py contributions to the absorption spectra are additive. They scale with the number of ligands.

In the resonance Raman effect, multiple states contribute at the polarizability level, eqs 13 and 14, and cross-terms appear in defining the cross-section. Myers et al.[3] included two states in modeling resonance Raman profiles of alkyl iodides, and Sension and Strauss[1] in modeling I$_2$. In the latter, I$_2$ is assumed to be cylindrical, with a diagonalizable polarizability tensor containing tensor components, γ and β. The γ component lies along the diatomic bond, and β, which is doubly degenerate, is perpendicular.

The resonantly enhanced A_1 vibrations of bpy are similar whether the ligand is isolated in Li$^+$bpy$^-$ or complexed in [Os(bpy)$_3$]$^{2+}$.[58,59] However, the magnitude of the resonance enhancement depends on the probability of the coupled electronic transition and both bpy and py MLCT transitions must be included. The symmetries of the electronic transitions thus correspond to the molecular symmetries, D$_3$ for ([Os(bpy)$_3$]$^{2+}$), C_2 for ([Os(bpy)$_2$(py)$_2$]$^{2+}$), and C_{2v} for ([Os(bpy)(py)$_4$]$^{2+}$). A simplified polarizability tensor model was developed that could distinguish the global symmetries of the three complexes, but which allowed for the calculation of Raman intensities.

As illustrated in Figure 4, the cylindrical model of Sension and Strauss[1] is sufficiently complex to distinguish the three different ligand sets. The tensors describing the cylinders at the right of Figure 4 were used to represent the MLCT transitions. On the left side of Figure 4, the diagonal *xx*, *yy*, and *zz* tensor components are given in terms of the bpy (ϕ_{b}) and py (ϕ_{p}) transitions. For [Os(bpy)$_3$]$^{2+}$, all components are bpy-based, $\alpha = 1/\sqrt{3}(\phi_{\mathrm{b1}} + \phi_{\mathrm{b2}} + \phi_{\mathrm{b3}})$. The Placzek invariants, eq 13, were then used in eq 14 to calculate differential Raman cross-section in ϕ_{b} and ϕ_{p}. The final expression for [Os(bpy)$_3$]$^{2+}$ is given by

$$\left(\frac{\mathrm{d}\sigma}{\mathrm{d}\Omega}\right)_{\parallel+\perp} = D\left(\frac{5}{4}(\phi_{\mathrm{b}})^2\right)$$

$$D = \frac{4\hbar_{\mathrm{s}}{}^3\hbar_{\mathrm{L}}e'_2}{15\hbar^4c^4} \tag{17}$$

Two py transitions define the γ axis for [Os(bpy)$_2$(py)$_2$]$^{2+}$ which is doubly degenerate because there are two py ligands. Two bpy ligands define the doubly degenerate β axes, and the tensor is given by, $\alpha = 1/\sqrt{2}(\phi_{\mathrm{b1}} + \phi_{\mathrm{b2}}) + 1/\sqrt{2}(\phi_{\mathrm{p1}} + \phi_{\mathrm{p2}})$ with

$$\left(\frac{\mathrm{d}\sigma}{\mathrm{d}\Omega}\right)_{\parallel+\perp} = D\left(\frac{9}{8}(\phi_{\mathrm{b}})^2 + 2(\phi_{\mathrm{p}})^2 + \frac{1}{4}(\phi_{\mathrm{b}}\,\phi^*{}_{\mathrm{p}} + \phi_{\mathrm{p}}\,\phi^*{}_{\mathrm{b}})\right) \tag{18}$$

For [Os(bpy)(py)$_4$]$^{2+}$, the single Os-bpy axis was taken as the γ axis and the py transitions as the doubly degenerate β axes, each of which is itself doubly degenerate. The tensor is

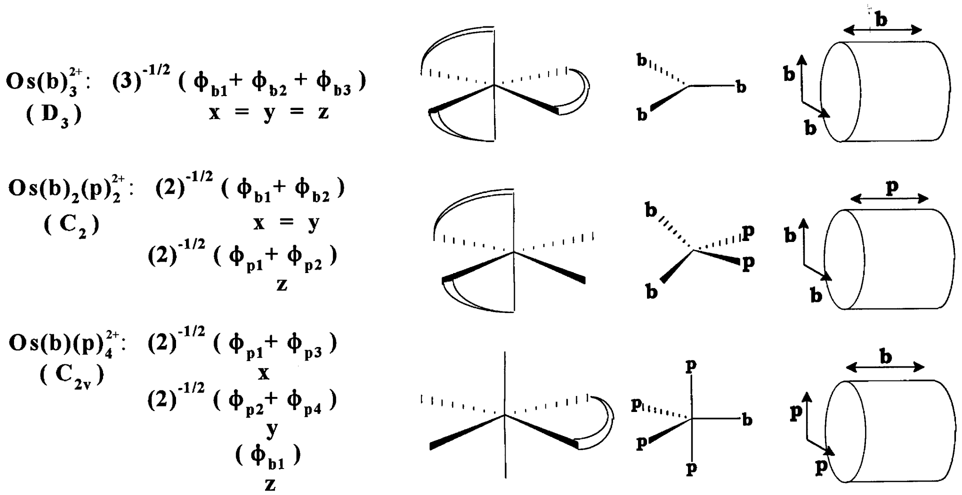

Figure 4. Illustration of the contributions to the Raman polarizability tensor for $[Os(bpy)(py)_4]^{2+}$, $[Os(bpy)_2(py)_2]^{2+}$, and $[Os(bpy)_3]^{2+}$ based on cylindrical geometry, far right. The cylinder axes are labeled bpy or py, based on the overall symmetry of the complexes. Off-diagonal components of the tensor are taken to be equal to 0, and diagonal components, x, y, and z, are assigned as bipyridine or pyridine, far left, based on cylindrical geometry. Normalized contributions are based on bpy and py MLCT transitions such that one bpy transition is spatially equivalent to two pyridine transitions.

given by $\alpha = 1/\sqrt{2}(\phi_{p1} + \phi_{p2}) + 1/\sqrt{2}(\phi_{p1} + \phi_{p2}) + \phi_{b1}$, and

$$\left(\frac{d\sigma}{d\Omega}\right)_{\|+\perp} = D\left((\phi_b)^2 + \frac{9}{2}(\phi_p)^2 + \frac{1}{2\sqrt{2}}(\phi_b\,\phi_p{}^* + \phi_p\,\phi_b{}^*)\right) \tag{19}$$

The two state analysis is required only for those bpy and py modes at 1606, 1015, and 1006 cm^{-1} that have the same or similar frequencies. For enhancements arising from bpy-based MLCT states, $\phi_p = 0$.

In the series $[Ru(bpy)_{3-n}(dmb)_n]^{2+}$ ($n = 0-3$ and dmb = 4,4′-dimethyl-2,2′-bipyridine), studied by Kincaid and coworkers,[66] vibrational intensity variations for the bpy and dmb ligands were attributed to differences in the energies of the bpy- and dmb-based MLCT transitions. This conclusion was based on data acquired at a single excitation wavelength and assumed a single excited state. This approach was justified by the electronic similarity of the dmb and bpy ligands. The bpy and py ligands are sufficiently different both vibrationally and electronically to merit the two-state model applied here.

Spectral Fitting Procedures and Protocols. The spectral fitting approach[36,46,67] that we adopted began with eqs 3 and 4 and 7 and 8 and involved fitting the lowest ^{1}MLCT absorption region and the resonance Raman excitation profiles. The 0−0 energy gap, E_0, is the origin of the vibrational progressions and it was used to optimize the profile on the energy axis. Vibrational frequencies were taken from Raman spectra. Estimates for the S_j values were made from the simple Heller relation (Savin formula)[21,40−42]

$$\frac{I_j}{I_*} = \frac{\omega_j^2 S_j}{\omega_*^2 S_*} \tag{20}$$

in which relative displacements are proportional to the measured Raman intensities. Individual mode intensities were varied, but less than 10%, to give “best fit” results (by eye). Inhomogeneous broadening, σ, was initially set to zero and optimized after optimization of the other parameters. The transition moment, M, was adjusted to fit the heights of both the Raman profiles and absorption spectra. After optimization including homogeneous broadening, inhomogeneous broadening, σ, was introduced and the spectral fits re-optimized by varying Γ, σ, M, and S_j. Results are summarized in Table 3 with ^{1}MLCT absorption fits shown in Figure 1S and Raman excitation profiles in Figure 2 and Figures 3S and 4S.

In fitting room-temperature emission band shapes, it was assumed that emission is from a single emitting MLCT state with bpy as the acceptor ligand.[22,23,68] The parameters obtained in the Raman and absorption fits were used, and the energy gap, E_0, allowed the variation to obtain the best fits as shown in Figure 3.

TABLE 3: Spectral Fitting Parameters[a,b] for Absorption and Raman in Water at 23 °C

$Os(bpy)(py)_4{}^{2+}$		$Os(bpy)_2(py)_2{}^{2+}$		$Os(bpy)_3{}^{2+}$	
$E_{0,bpy} = 20{,}750\ cm^{-1}$ $E_{0,py} = 22{,}350\ cm^{-1}$		$E_{0,bpy} = 20{,}850\ cm^{-1}$ $E_{0,py} = 22{,}350\ cm^{-1}$		$E_{0,bpy} = 20{,}850\ cm^{-1}$	
$\hbar\omega_j$ (cm^{-1})	S_j	$\hbar\omega_j$ (cm^{-1})	S_j	$\hbar\omega_j$ (cm^{-1})	S_j
1606	0.080	1606	0.060	1606	0.063
	(0.070)		(0.060)		
1558	0.140	1558	0.128	1558	0.125
1485	0.225	1485	0.273	1485	0.266
1323	0.070	1323	0.071	1323	0.073
1265	0.025	1265	0.041	1265	0.049
1218	(0.090)	1218	(0.012)		
1174	0.045	1174	0.065	1174	0.062
1108	0.004			1108	0.002
1066	0.006	1066	0.002		
1053	0.004	1036	0.009	1049	0.004
1030	0.020	1025	0.015	1030	0.028
1015	0.015	1011	0.014	1015	0.010
	(0.008)		(0.011)		
1006	0.021				
	(0.015)				
666	0.018	670	0.017	669	0.019
375	0.016	375	0.018	375	0.014
280	0.012	280	0.005	[280	0.006][c]

[a] Pyridine displacements are given in parentheses. [b] Other parameters, the same for all three complexes, are $M_{bpy} = 0.55$ Å, $M_{py} = 0.34$ Å, $\sigma = 720\ cm^{-1}$, $\Gamma = 255\ cm^{-1}$, integration time = 800 fs., no. of time pts. = 950, no. of energy points = 500. [c] Difficult to observe experimentally; mode added for consistency.

TABLE 4: Single-mode Emission Spectral Fitting Parameters in Water at 23 °C

(a) Simplex Fitting Routine

	$[Os(bpy)(py)_4]^{2+}$	${}^a[Os(bpy)_2(py)_2]^{2+}$	${}^a[Os(bpy)_3]^{2+}$
E_0 (cm^{-1})	12 669	13 147	13 700
$\hbar\omega$ (cm^{-1})	1300	1300	1300
S	0.70	0.67	0.90
$\Delta\bar{v}_{1/2}$ (cm^{-1})	1703	2017	1526
λ_o (cm^{-1})	1271	1783	1021

(b) Average of Multi-Mode Raman Parameters[b]

	$[Os(bpy)(py)_4]^{2+}$	$[Os(bpy)_2(py)_2]^{2+}$	$[Os(bpy)_3]^{2+}$
E_0 (cm^{-1})	12 700	13 200	13 650
$\hbar\omega_{ave}$ (cm^{-1})	1357	1370	1369
S_{ave}	0.70	0.83	0.87
$\Delta\bar{v}_{1/2}$ (cm^{-1})	1799	1799	1799
λ_o (cm^{-1})	1419	1419	1419

[a] For comparison, spectral fitting results from ref 23 for $[Os(bpy)_3]^{2+}$ and $[Os(bpy)_2(py)_2]^{2+}$ were $E_0 = 13510$ and 13080 cm^{-1}, $S = 0.75$ and 0.65, and $\Delta\bar{v}_{1/2} = 1550$ and 1580 cm^{-1}, respectively, with $\hbar\omega = 1300$ cm^{-1}. [b] Single-mode averages of the multi-mode parameters in Table 3, calculated from eq 21 and used to calculate the spectra in Supplementary Figure 5.

TABLE 5: Seven Mode Average Parameters for the Data in Figure 6[a]

$[Os(bpy)(py)_4]^{2+}$	$[Os(bpy)_2(py)_2]^{2+}$	$[Os(bpy)_3]^{2+}$
$E_0 = 12\ 700$ cm^{-1}	$E_0 = 13\ 200$ cm^{-1}	$E_0 = 13\ 650$ cm^{-1}
$\hbar\omega_j$ (cm^{-1}), S_j	$\hbar\omega_j$ (cm^{-1}), S_j	$\hbar\omega_j$ (cm^{-1}), S_j
1575, 0.220	1572, 0.216	1574, 0.226
1485, 0.225	1485, 0.314	1485, 0.320
1308, 0.095	1302, 0.129	1300, 0.146
1174, 0.050	1174, 0.075	1174, 0.074
1038, 0.070	1024, 0.046	1032, 0.053
666, 0.018	670, 0.020	669, 0.023
334, 0.028	354, 0.026	346, 0.024

[a] Other parameters used in the calculation of nonradiative rate constants (eq 30) included $\Delta\bar{v}_{1/2} = 1799$ cm^{-1} ($\lambda_0 = 1419$ cm^{-1}).

Triplet normal-mode frequencies have been observed to differ slightly from the corresponding singlet states frequencies by time-resolved resonance Raman spectroscopy and by direct spectral comparisons.[60,63,69,70] The differences are small and ground-state frequencies were used in fitting the emission spectra. To account for the possibility of mode displacement changes between singlet and triplet states, a constant multiplier of the S_j values derived from the excitation profiles, c, was used as a variable parameter in fitting the emission spectrum. This procedure kept relative displacements constant while allowing the overall S values to vary, see below.

The solvent broadening parameters were kept the same for absorption, Raman, and emission for all three complexes. Best fits were obtained in the slow modulation limit of homogeneous broadening (Gaussian) and by using a Gaussian form for the inhomogeneous broadening.

Eq 10 was used to equate radiative rate constants (k_r) in Table 2 with calculated emission manifolds, with M_{em} being the only adjustable parameter. The values of M_{em} that resulted for each of the calculations are listed in Table 6.

Normal-Mode Averaging. The resonance Raman experiment provides the mode-specific parameters necessary to calculate vibrational contributions to radiative and nonradiative decay. In high-temperature spectra, solvent broadening and a multiplicity of contributors convolutes individual mode progressions. It has been suggested that all the requisite information is present in averaged band shapes to calculate the vibrational overlap factors for radiative and nonradiative decay.[17−25,46] This is an important point, because using average parameters from normalized absorption and emission band shapes is far simpler than interpreting and calculating these quantities with mode-specific resonance Raman data.

In the average mode approximation, multiple modes are represented by an average frequency, $\hbar\omega$, and dimensionless displacement, S, given by[23,25−28]

$$\hbar\omega = \frac{\sum_j \hbar\omega_j S_j}{\sum_j S_j}$$

$$S = \sum_j S_j \tag{21}$$

Eq 21 is obtained by assuming that the individual vibronic peaks are well-represented as Gaussians with half-widths greater than the spread in vibrational frequencies. When the sum over j included all coupled modes, the average frequency was ∼1350 cm^{-1}, the progression observed in low-temperature emission. The “missing mode” or MIME effect is a rigorous time-dependent method for calculating observed progressions from the individual modes that are their origin.[61,62,71,72]

Many important correlations between theory and experiment have been made based on one- and two-mode spectral fits. The single-mode expression for emission spectral fitting[29,30,35,38] in terms of the emission intensity, $I(\nu)$, relative to the intensity of the 0−0 transition, is given by eq 22

$$\frac{I(\bar{v})}{I_{0-0}} = \sum_v \left[\left(\frac{E_0 - v\hbar\omega}{E_0}\right)^3 \frac{S^v}{v!} \times \exp\left(-4\ln 2\left(\frac{\bar{v} - E_0 + v\hbar\omega}{\Delta\bar{v}_{1/2}}\right)^2\right)\right] \tag{22}$$

In eq 22, v is the vibrational quantum number in the ground state with vibrational frequency $\hbar\omega$ and displacement S. E_0 is the energy of the $v^* = 0 \rightarrow v = 0$ transition, and $\Delta\bar{v}_{1/2}$ (cm^{-1}) is the full-width at half-maximum of the individual vibronic components. As written, $\Delta\bar{v}_{1/2}$ contains contributions from the solvent as well as low- frequency vibrations treated classically. The homogeneous (Γ) and inhomogeneous (σ) solvent broadening terms, eqs 5 and 6, are related to the full-width at half-maximum $\Delta\bar{v}_{1/2}$ in eq 22 by eq 23

$$\Delta\nu_{1/2} = (8\ln 2)^{1/2}\,(\sigma + \sqrt{2}\,\Gamma) \tag{23}$$

One-mode emission spectral fits were conducted with $\hbar\omega = 1300$ cm^{-1}, consistent with previous analyses.[22,23,26,28] Fitting to eq 22 utilized a simplex minimization routine which automatically obtains a least-squares fit to the experimental data, provides statistical information, and greatly simplifies the fitting procedure.[73,74] The resulting fitting parameters are listed in Table 4a, and spectra and calculated fits are shown in Figure 5S. Transition moments calculated by using single-mode spectral fitting parameters to calculate the integral in eq 10 and experimental k_r values are listed in Table 6.

These results are compared with those obtained by applying the one-mode fitting procedure to an “averaged” single-mode representation of the multi-mode parameters from the Raman/

TABLE 6: Transition Moments and Electronic Matrix Elements for Nonradiative Decay

origin	$Os(bpy)(py)_4^{2+}$	$Os(bpy)_2(py)_2^{2+}$	$Os(bpy)_3^{2+}$
absorption/Raman, ^{1}MLCT			
multi-mode[a]	$M_{bpy} = 0.55$Å	$M_{bpy} = 0.55$Å	$M_{bpy} = 0.55$Å
	$M_{py} = 0.34$Å	$M_{py} = 0.34$Å	$M_{py} = 0.34$Å
radiative decay, ^{3}MLCT			
multi-mode[b]	$M_{em} = 0.050$ Å	$M_{em} = 0.042$ Å	$M_{em} = 0.040$ Å
averaged, one-mode[c]	$M_{em} = 0.050$ Å	$M_{em} = 0.042$ Å	$M_{em} = 0.042$ Å
simplex, ^{1}one-mode[d]	$M_{em} = 0.044$ Å	$M_{em} = 0.041$ Å	$M_{em} = 0.040$ Å
nonradiative decay, ^{3}MLCT			
seven-mode[e]	$V_k = 755$ cm^{-1}	$V_k = 804$ cm^{-1}	$V_k = 1177$ cm^{-1}
averaged, one-mode[f]	$V_k = 960$ cm^{-1}	$V_k = 845$ cm^{-1}	$V_k = 1215$ cm^{-1}
simplex, one-mode[f]	$V_k = 1602$ cm^{-1}	$V_k = 942$ cm^{-1}	$V_k = 2213$ cm^{-1}

[a] Calculated by using parameters from Table 3, eq 7, eq 10, and k_r from Table 2. [b] Calculated by using parameters from Table 3, eq 10, and k_r from Table 2 with E_0 and c values listed in the text. [c] Same as *b* but with parameters averaged to one mode by using eq 21. [d] Simplex minimization routine, with single mode $\hbar\omega = 1300$ cm^{-1}. [e] Calculated from experimental k_{nr} values and eq 30 with the parameters in Table 5. [f] As in *e* but by using eq 28 and parameters in Table 4.

absorption fits (Table 3). Spectral fits are shown in Figure 5S and transition moments are listed in Table 6.

Electronic Coupling Matrix Elements for Radiative and Nonradiative Decay. The rate constant for radiative decay, k_r, is given by eq 24

$$k_r = A = 8\pi hcn^3\langle\bar{v}^{-3}\rangle^{-1}B \qquad (24)$$

with

$$B = \left(\frac{8\pi^3}{3h^2c}\right)\left\langle\frac{e^2M^2}{4\pi\epsilon_0}\right\rangle = \left(\frac{2303}{hnN_A}\right)\int\epsilon(\bar{v})\mathrm{d}\ln\bar{v} \qquad (25)$$

In eq 25, e is the unit electron charge, ϵ_0 is the permittivity of a vacuum, c is the speed of light, N_A is Avogadro's number, and M is the transition moment in units of distance. (In an earlier paper,[23] $\hbar$ rather than h appears in these expressions.)[25,75] In eq 24, n is the refractive index of the solvent, and $\langle\bar{v}^{-3}\rangle^{-1}$ is the inverse of the cube of the average emission energy $\bar{v}^{-3}$ (in units of cm^{-1}) for the emission profile, which can be evaluated analytically by using eq 26

$$\langle\bar{v}^{-3}\rangle^{-1} = \frac{(\int I(\bar{v})\mathrm{d}\bar{v})}{\left(\int\frac{I(\bar{v})}{\bar{v}^3}\mathrm{d}\bar{v}\right)} \qquad (26)$$

In eq 26, $I(\bar{v})$ is the emission intensity at $\bar{v}$ in photons cm^{-1} s^{-1}.

In an earlier study involving ~30 [Os(bpy, phen)L$_4$]$^{n+}$ complexes, including the three in this study, it was assumed that the transition moment would remain relatively constant, given the common orbital basis ($d\pi^5\pi^{*1}$) for the Os^{III}(bpy$^{-}\cdot$) or Os^{III}(phen$^{-}\cdot$) MLCT excited states. With this assumption, an average M_{em}^2 value was evaluated from the slope of a plot of k_r versus $\langle\bar{v}^{-3}\rangle^{-1}$, which gave $M_{em} = 0.049$.[23,76] It is also possible to evaluate M_{em}^2 by using the time-dependent formalism and eq 10. In this approach, the magnitude of M_{em}^2 is equal to the slope of a plot of k_r versus FC,[76] with

$$\mathrm{FC} = \frac{2n}{3\pi\hbar^5c^3}\int E_S^3F(E_S)\mathrm{d}E_S \qquad (27)$$

E_s^3 $F(E_s)$ is defined in eq 9 in terms of the spectral fitting parameters. Values of FC were calculated from the one-mode spectral fitting parameters for the 32 complexes in the earlier study.[23] From the slope of a plot of k_r versus FC, $M_{em} = 0.068$.

In the limits $E_0 \gg S\hbar\omega$ and $\hbar\omega \gg k_BT$ for the single-mode approximation, application of time-dependent perturbation theory with application of the "Golden Rule" leads to the Energy Gap Law for nonradiative decay.[19−23,77] It relates the rate constant for nonradiative decay, k_{nr}, to the free energy change, $\Delta G°$, as shown in eq 29

$$\ln(k_{nr}) = \ln(\beta_0) + \ln(F_{calc}) \qquad (28)$$

where

$$\beta_0 = \frac{V_k^{\,2}(2\pi)^{1/2}}{\hbar} \qquad (29a)$$

$$\ln(F_{calc}) = -\frac{1}{2}\ln(\hbar\omega E_0) - S - \frac{\gamma E_0}{\hbar\omega} + \frac{(\gamma+1)^2}{16\ln 2}\left(\frac{\Delta\bar{v}_0}{\hbar\omega}\right)^2 \qquad (29b)$$

$$\gamma = \ln\left(\frac{E_0}{S\hbar\omega}\right) - 1 \qquad (29c)$$

and

$$E_0 = |\Delta G°| - \lambda \qquad (29d)$$

In eq 29a, V_k is the vibrationally induced electronic coupling matrix element. A related form of eq 29 has been used to account for electron transfer in the inverted region.[22,26,77−80]

If it is assumed that the frequency factor β_0, eq 28, is constant through the series of Os complexes alluded to above, V_k can be evaluated from the slope of a plot of ln(k_{nr}) vs ln(F_{calc}). This analysis[23] gave $\beta = -34.3$ and $V_k = 1300$ cm^{-1}, assuming a promoting mode quantum spacing of 300 cm^{-1} with an error range of 750−2250 cm^{-1} for V_k.

Including multiple coupled modes, k_{nr} is given by the sum-over-energy-states expression[77] in eq 30. Attempts to encode eq 11 on the computer did not result in meaningful results.[81]

$$k = \frac{2\pi V_k^{\,2}}{\hbar}\left(\frac{1}{4\pi\lambda_o k_b T}\right)^{1/2} \exp\left(-\sum_j S_j \coth\left(\frac{\hbar\omega_j}{2k_b T}\right)\right) x$$

$$\prod_j \sum_{m_j}\left(\exp\left(\frac{m_j\hbar\omega_j}{2k_b T}\right) I_{mj}\left[S_j \csc h\left(\frac{\hbar\omega_j}{2k_b T}\right)\right] \times \exp\left(\frac{-(\Delta G^0 + \lambda + \sum_j m_j\hbar\omega_j)}{4\lambda_o k_b T}\right)\right) \qquad (30a)$$

$$I_{mj}(z) = \left(\frac{z}{2}\right)^{m_j} \sum_{k=0}^{\infty} \frac{\left(\frac{z^2}{4}\right)^k}{k!(m_j + k)!} \qquad (30b)$$

$$|\Delta G^0| = E_0 + \lambda_0 \qquad (30c)$$

In this expression, λ_o is the solvent reorganizational energy. It is related to the spectral full-width at half-maximum, $\Delta\bar{v}_{1/2}$, by

$$\lambda_o = \frac{(\Delta\bar{v}_{1/2})^2}{16k_b T \ln 2} \qquad (31)$$

The other parameters in eq 30 have all been described previously. The vibrationally induced electronic matrix element, V_k (in cm^{-1}), is the only parameter not determined by the spectral fitting procedure.

To simplify the calculation, the multi-mode information was represented by seven "average" modes obtained by application of eq 21, Table 5. Vibrational contributions to k_{nr} were calculated both by using eq 30 and the parameters in Table 5, and the single-mode parameters in Table 4. Values for V_k were calculated from the experimental k_{nr} values and either eq 28 or 30 and are listed in Table 6.

Discussion

The vibrational information required to calculate vibrational overlap contributions to the kinetics of excited-state processes resides in emission and absorption spectral profiles. However, at or near room temperature, broadening and spectral overlap obviate the ability to discern individual mode contributors. A standard procedure in treating such data is to use single- or double-mode approximations to analyze the spectral profiles.

Resonance Raman provides the information required to represent individual modes explicitly. An important question is whether there is a convergence between the simplified and mode-for-mode Raman analyses, and if so, at what level. One of the goals of this work was to compare the calculational results obtained by the two approaches in order to judge how well they compare in providing accurate kinetic parameters for excited-state decay.

A large number of parameters are involved in the mode-for-mode analysis of large molecules with multiple coupled vibrations. When resonance enhancement occurs from a single electronic state, the nine-element polarizability matrix collapses to a single element along the direction of the transition dipole. If two or more states contribute, they interfere, and the symmetry of the molecule and the contributing transition dipoles must be included in the analysis.

The cylindrical model applied here was applied previously to two-state interference effects in resonance Raman scattering.[1,3] Due to the ligand-centered, charge-transfer character of the excitations in the Os(II) complexes, the dimensions of the cylinder are associated with bpy- or py-type MLCT transitions, and Raman contributions are easily distinguished vibronically. While the cylindrical model is limited in its representation of the symmetry of the complexes, it does distinguish the three complexes and is simple enough to be calculationally tractable. It also results in reasonable solvent and vibrational parameters.

For $[Os(bpy)_3]^{2+}$, the initial fitting procedure involved analysis of 13 total band shapes (one absorption profile and 12 Raman excitation profiles). The normal-mode frequencies were taken from the Raman spectra, and the initial set of relative S_j values calculated from the experimental intensities and the Heller relationship in eq 20. The relative values were subsequently adjusted to fit the profiles. This left four independent parameters, E_0, Γ, σ, and the constant multiplier of the S_j values to be determined.

On the basis of the Strickler–Berg relationship,[25] vibrational parameters derived from absorption/Raman spectra should apply directly to emission and nonradiative decay, but only if absorption and emission interconvert the same states. At the excitation wavelengths used for the Os(II) complexes, resonance Raman scattering is observed from transitions to ^{1}MLCT state(s), which decay on the 100's of fs time scale.[82] Emission occurs on the nanosecond time scale from thermally equilibrated ^{3}MLCT states. It was not possible experimentally to observe resonance Raman enhancement from the triplets because of competing emission.

Spectral Parameters. E_0, $\hbar\omega$, S. In our analysis, it was assumed that the vibrational frequencies for singlet and triplet states were the same. *Average* singlet and triplet frequencies are very nearly the same.[63,69,70] We also assumed that the relative equilibrium displacements of the singlet and triplet frequencies were the same, even if the sum of the displacements varied.

The comparisons in Table 4 show that comparable values of S are obtained from: (1) the one-mode emission spectral fitting analysis and (2) S_{ave} calculated from the S_j values in Table 3 and the averaging procedure in eq 21. Similarly, the values of $\hbar\omega_{ave}$ calculated from the multi mode data and the averaging procedure (1357, 1370, and 1369 cm^{-1}) justify the assumption of $\hbar\omega = 1300$ cm^{-1} in the emission spectral fitting.

These comparisons and the good agreement between E_0 values obtained by the two procedures support the validity of the approximate single-mode analysis in acquiring reasonably accurate information about the MLCT excited states.

The magnitudes of the S and E_0 values for the three complexes in the series are also revealing. There is a slight trend toward a higher S value that parallels the increase in E_0 as the number of bpy ligands increases, suggesting that the pyridyl ligands may be better ancillary electron donors than bpy.

A common solvent reorganizational energy, λ_o, was also assumed independent of ligand set in the absorption, emission and Raman analysis. This had the effect of forcing differences in λ_o between complexes and between the absorption/Raman and emission analyses to appear in the S_j values or the average value S. The slow modulation limit was assumed for homogeneous broadening and a Gaussian distribution for inhomogeneous broadening.[4,58,59]

As can be seen from the data in Table 4, there is only marginally good agreement between this value, $\Delta\bar{v}_{1/2} = 1800$ cm^{-1}, $\lambda_0 = 1410$ cm^{-1}, and $\lambda_0 = 1263$, 1771, and 1014 cm^{-1} for the three complexes from emission spectral fitting.

Transition Moments, M_{bpy}, M_{py}, and M_{em}, and Vibrationally Induced Electronic Coupling Matrix Elements, V_k.

Due to the common orbital origins of the ground and excited states, common bpy and py transition moments were assumed. The singlet → singlet transition moments derived from the absorption and Raman fitting procedures were $M_{\text{bpy}} = 0.55$ Å and $M_{\text{py}} = 0.34$ Å, Table 3. The latter is less certain because of the absence of a maximum in the py-based Raman excitation profiles. These values are close in magnitude to those calculated for $\pi - \pi$ transitions in a series of organics by Strickler and Berg.[25]

Transition moments for emission, M_{em}, were calculated by using experimental k_{r} values and eq 10. The resulting moments are an order of magnitude smaller than for absorption, consistent with the singlet character of the ground state and the triplet character of the emitting excited state. Values obtained by using various fitting procedures to calculate the spectral overlap integral in eq 10 are listed in Table 6.

The values of M_{em} in Table 6 are relatively independent of the fitting procedure used to calculate them. Within experimental error, they agree with the value of 0.068 obtained earlier for the extended series of osmium complexes.[23]

With transition moments and spectral fitting parameters available, it is possible to calculate the contribution of the GS→^{3}MLCT transition to the low energy absorption spectrum ($\sim$13 000 to 18 000 cm^{-1}). For the extended series of Os$^{\text{II}}$ complexes alluded to above,[23] a calculated absorption band for the lowest-energy ^{3}MLCT transition was predicted to occur at $\sim$15 000 cm^{-1} (667 nm) with $\epsilon = 400$ L M^{-1} cm^{-1} and $\Delta\bar{\nu}_{1/2} = 300$ cm^{-1}, assuming a Gaussian band shape. On the basis of the average emission parameters from Table 4b and $E_{\text{abs}} = E_{0,\text{em}} + 2\lambda_{\text{o}}$, application of eq 28 from ref 23 gives E_{abs} values on the order of 16 000 cm^{-1} and $\epsilon \sim 65$ L M^{-1} cm^{-1}. The experimental molar absorptivity in this energy region is more than an order of magnitude larger, $\sim$5000 M^{-1} cm^{-1}. The ^{3}MLCT absorption estimate is based on a single, averaged ^{3}MLCT emissive state. The ^{3}MLCT absorption band is also overlapped with absorptions at higher energies, making it difficult to compare theoretical and experimental values.

The values of V_k in Table 6 were calculated from the experimental rate constants, k_{nr}, eq 28, and the kinetic parameters in Table 4 or 5. The spread in values with $V_k = 750-1200$ cm^{-1} (900 cm^{-1} average) from the multi-mode fits is relatively small. Values calculated from the single-mode emission spectral fitting parameters were in the range 940−2200 cm^{-1} (1600 cm^{-1} average). Both are consistent with $\langle V_k \rangle = 1300$ cm^{-1} from the previous study.[23]

Conclusions

We have interpreted resonance Raman excitation profiles by using a simplified two-state interference model, incorporating both bpy and py MLCT transitions in a series of mixed-ligand pyridyl-polypyridyl complexes. A simplified cylindrical model for the complexes was applied, which fits the data reasonably well.

The results of the Raman analysis have been applied to the calculation of absorption and emission spectra. They have also been used to calculate spectral overlap integrals and Franck−Condon factors. From these quantities and experimental radiative and nonradiative decay rate constants, transition moments for emission and electronic coupling matrix elements for vibrationally induced nonradiatuve decay have been calculated.

There appears to be no statistically significant difference between using the explicit multi-mode information obtained from the Raman analysis and “average” mode information obtained by emission spectral fitting, at least at room temperature. This includes the parameters S and $\hbar\omega$, transition moments, and electronic coupling matrix elements. There is satisfaction in devising a detailed model that encompasses the complexity of the three Os-polypyridine complexes and fits the dozens of spectral profiles (Raman, absorption, and emission) using existing time-dependent theory. These complexes have provided an experimental arena in which the theoretical relationships between spectral profiles and excited-state kinetics could be explored. While a full fitting of Raman excitation profiles provides valuable mode-specific information about the resonant electronic transition, there is adequate vibronic information in absorption and emission spectra alone, at least at room temperature, to obtain the parameters that characterize MLCT excited-state energies, distortions, and the dynamic quantities that dictate excited-state decay.

Acknowledgment. Thanks to Ed Kober for many helpful discussions. Much appreciation to Steve Doorn and Dave Morris for early copies of their computer programs and for later helpful discussions. T.J.M. acknowledges funding from US DOE grant #DE-FG02-96ER 14607.

Supporting Information Available: Five supplementary figures (Figures 1S−5S) are available to the interested reader. The material is available free of charge via the Internet at http://pubs.acs.org.

References and Notes

(1) Sension, R. J.; Strauss, H. L. *J. Chem. Phys.* **1986**, *85*, 3791.
(2) Clark, R. J. H.; Stead, M. J. *Inorg. Chem.* **1983**, *22*, 1214.
(3) Phillips, D. L.; Myers, A. B. *J. Chem. Phys.* **1991**, *95*, 226.
(4) Markel, F.; Ferris, N. S.; Gould, I. R.; Myers, A. B. *J. Am. Chem. Soc.* **1992**, *114*, 6208.
(5) Wynne, K.; Galli, C.; Hochstrasser, R. M. *J. Chem. Phys.* **1994**, *100*, 4797.
(6) Doorn, S. K.; Hupp, J. T. *J. Am. Chem. Soc.* **1989**, *111*, 4704.
(7) Blackbourn, R. L.; Johnson, C. S.; Hupp, J. T.; Bryant, M. A.; Sobocinski, R. L.; Pemberton, J. E. *J. Phys. Chem.* **1991**, *95*, 10535.
(8) Kliner, D. A. V.; Tominga, K.; Walker, G. C.; Barbara, P. F. *J. Am. Chem. Soc.* **1992**, *114*, 8323.
(9) Loppnow, G. R.; Mathies, R. A. *Biophys. J.* **1988**, *54*, 35.
(10) Myers, A. B.; Harris, R. A.; Mathies, R. A. *J. Chem. Phys.* **1983**, *79*, 603.
(11) Kodama, K.; Bandrauk, A. D. *Chem. Phys. Lett.* **1981**, *80*, 248.
(12) Sweeney, J. A.; Asher, S. A. *J. Phys. Chem.* **1990**, *94*, 4784.
(13) Dallinger, R. F. *J. Am. Chem. Soc.* **1985**, *107*, 7.
(14) Doorn, S. K.; Blackborn, R. L.; Johnson, C. S.; Hupp, J. T. *Electrochim. Acta* **1991**, *36*, 1775.
(15) Blackbourn, R. L.; Johnson, C. S.; Hupp, J. T. *J. Am. Chem. Soc.* **1991**, *113*, 1060.
(16) Tominga, K.; Kliner, D. A. V.; Johnson, A. E.; Levinger, N. E.; Barbara, P. F. *J. Chem. Phys.* **1993**, *98*, 1228.
(17) Ulstrup, J.; Jortner, J. *J. Chem. Phys.* **1975**, *63*, 4358.
(18) Lin, S. H.; Colangelo, L. J.; Eyring, H. *Proc. Nat. Acad. Sci.* **1971**, *68*, 2135.
(19) Engleman, R.; Jortner, J. *Mol. Phys.* **1970**, *18*, 145.
(20) Freed, K. F.; Jortner, J. *J. Chem. Phys.* **1970**, *52*, 6272.
(21) Heller, E. J.; Brown, R. C. *J. Chem. Phys.* **1983**, *79*, 3336.
(22) Caspar, J. V.; Kober, E. M.; Sullivan, B. P.; Meyer, T. J. *J. Am. Chem. Soc.* **1982**, *103*, 7480.
(23) Kober, E. M.; Caspar, J. V.; Lumpkin, R. S.; Meyer, T. J. *J. Phys. Chem.* **1986**, *90*, 3722.
(24) Orlandi, G.; Monti, S.; Balzani, V. *Chem. Phys.* **1980**, *52*, 313.
(25) Strickler, S. J.; Berg, R. A. *J. Chem. Phys.* **1962**, *37*, 814.
(26) Chen, P. Y.; Duesing, R.; Graff, D. K.; Meyer, T. J. *J. Phys. Chem.* **1991**, *95*, 5850.
(27) Engel, P. S.; Fogel, L. D.; Steel, C. *J. Am. Chem. Soc.* **1974**, *96*, 327.
(28) Murtaza, Z.; Graff, D. K.; Zipp, A. P.; Worl, L. A.; Jones, W. E.; Bates, W. D.; Meyer, T. J. *J. Phys. Chem.* **1994**, *94*, 10504.
(29) Kober, E. M.; Marshall, J. L.; Dressick, W. J.; Sullivan, B. P.; Caspar, J. V.; Meyer, T. J. *Inorg. Chem.* **1985**, *24*, 2755.
(30) Lumpkin, R. S.; Meyer, T. J. *J. Phys. Chem.* **1986**, *90*, 5307.
(31) Caspar, J. V.; Sullivan, B. P.; Kober, E. M.; Meyer, T. J. *Chem. Phys. Lett.* **1982**, *91*, 91.

(32) Denti, G.; Campagna, S.; Serroni, S.; Ciano, M.; Balzani, V. *J. Am. Chem. Soc.* **1992**, *113*, 2944.

(33) Richter, M. M.; Brewer, K. J. *Inorg. Chem.* **1993**, *32*, 5762.

(34) Bryant, G. M.; Fergusson, J. E.; Powell, H. K. J. *Aust. J. Chem.* **1971**, *24*, 257.

(35) Myers, A. B.; Li, B.; Ci, X. *J. Chem. Phys.* **1988**, *89*, 1876.

(36) Myers, A. B.; Mathies, R. A.; Tannor, D. J.; Heller, E. J. *J. Chem. Phys.* **1982**, *77*, 3857.

(37) Dudik, J. M.; Johnson, C. R.; Asher, S. A. *J. Chem. Phys.* **1985**, *82*, 1732.

(38) Myers, A. B.; Li, B. *J. Phys. Chem.* **1990**, *94*, 4051.

(39) Miller, P. J.; Chao, R. S. *J. Raman Spectrosc.* **1979**, *8(1)*, 17.

(40) Heller, E. J.; Sundberg, R. L.; Tannor, D. *J. Phys. Chem.* **1982**, *86*, 1822.

(41) Heller, E. J. *Acc. Chem. Res.* **1981**, *14*, 368.

(42) Lee, S.; Heller, E. J. *J. Chem. Phys.* **1979**, *71*, 4777.

(43) Myers, A. B.; Mathies, R. A. Chapter 1, Resonance Raman Intensities: A Probe of Excited-State Structure and Dynamics. In *Biological Applications of Raman Spectroscopy*; Spiro, T. G., Ed.; Wiley and Sons: New York, 1988; p 1.

(44) Kelley, A. M. *J. Phys. Chem. A* **1999**, *103*, 6891.

(45) Lilichenko, M.; Tittelbach-Helmrich, D.; Verhoeven, J. W.; Gould, I. R.; Myers, A. B. *J. Chem. Phys.* **1998**, *109(24)*, 10958.

(46) Myers, A. B. *Chem. Phys.* **1994**, *180*, 215.

(47) Mukamel, S. *Annu. Rev. Phys. Chem.* **1990**, *41*, 647.

(48) Myers, A. B.; Li, B. *J. Chem. Phys.* **1990**, *92*, 3310.

(49) Kulinowski, K.; Gould, I. A.; Myers, A. B. *J. Phys. Chem.* **1995**, *99*, 9017.

(50) Blazej, D. C.; Peticolas, W. L. *J. Chem. Phys.* **1980**, *72*, 3134.

(51) Stallard, B. R.; Champion, P. M.; Callis, P. R.; Albreacht, A. C. *J. Chem. Phys.* **1983**, *78*, 712.

(52) Nibbering, E. T. J.; Duppen, K.; Wiersma, D. A. *J. Photochem. Photobiol. A: Chem.* **1992**, *62*, 347.

(53) Mortenson, O. S.; Hassing, S. In *Advances in Infrared and Raman Spectroscopy*; Clark, R. J. H., Hester, R., Eds.; Heyden and Son Ltd.: London, 1980, Vol. 6, p 1.

(54) Wooton, J. L.; Zink, J. I. *J. Am. Chem. Soc.* **1997**, *119*, 1895.

(55) Siebrand, W.; Zgierski, M. Z. *J. Raman Spectrosc.* **1982**, *13*, 78.

(56) Kober, E. M.; Meyer, T. J. *Inorg. Chem.* **1982**, *21*, 3967.

(57) Pankuch, B. J.; Lacky, D. E.; Crosby, G. A. *J. Phys. Chem.* **1980**, *84*, 2061.

(58) Mallick, P. K.; Danzer, G. D.; Strommen, D. P.; Kincaid, J. R. *J. Phys. Chem.* **1988**, *92*, 5628.

(59) McClanahan, S.; Kincaid, J. R. *J. Raman Spectrosc.* **1984**, *15*, 173.

(60) Bradley, P. G.; Kress, N.; Kornberger, B. A.; Dallinger, R. F.; Woodruff, W. H. *J. Am. Chem. Soc.* **1981**, *103*, 7441.

(61) Tutt, L.; Zink, J. I. *J. Am. Chem. Soc.* **1986**, *108*, 5830.

(62) Johnson, C. S.; Mottley, C.; Hupp, J. T.; Danzer, G. D. *Inorg. Chem.* **1992**, *31*, 5143.

(63) Caspar, J. V.; Westmoreland, T. D.; Allen, G. H.; Bradley, P. G.; Meyer, T. J.; Woodruff, W. H. *J. Am. Chem. Soc.* **1984**, *106*, 3492.

(64) Felix, F.; Ferguson, J.; Gudel, H. U.; Ludi, A. *Chem. Phys. Lett.* **1979**, *62*, 153.

(65) Decurtins, S.; Felix, F.; Ferguson, J.; Gudel, H. U.; Ludi, A. *J. Am. Chem. Soc.* **1980**, *102*, 4102.

(66) McClanahan, S. F.; Dallinger, R. F.; Holler, F. J.; Kincaid, J. R. *J. Am. Chem. Soc.* **1985**, *107*, 4853.

(67) Myers, A. B. *Chem. Rev.* **1996**, *96*, 911.

(68) DeArmond, M. K.; Myrick, M. L. *Acc. Chem. Res.* **1989**, *22*, 364.

(69) Carroll, P. J.; Brus, L. E. *J. Am. Chem. Soc.* **1987**, *109*, 7613.

(70) Danzer, G. D.; Kincaid, J. R. *J. Phys. Chem.* **1990**, *94*, 3976.

(71) Tutt, L. W.; Zink, J. I.; Heller, E. J. *Inorg. Chem.* **1987**, *26*, 2158.

(72) Larson, L. J.; Zink, J. I. *Inorg. Chem.* **1989**, *28*, 3519.

(73) Lumpkin, R. S. Doctoral Dissertation, University of North Carolina at Chapel Hill, 1987.

(74) Claude, J. P. Doctoral Dissertation, University of North Carolina at Chapel Hill, 1995.

(75) Levine, I. N. *Molecular Spectroscopy*; John Wiley and Sons: New York, 1975.

(76) Graff, D. K. Doctoral Dissertation, University of North Carolina at Chapel Hll, 1994.

(77) Brunschwig, B. S.; Sutin, N. S. *Comm. Inorg. Chem.* **1987**, *6*, 209.

(78) Closs, G. L.; Calcaterra, L. T.; Green, N. J.; Penfield, K. W.; Miller, J. V. *J. Phys. Chem.* **1986**, *90*, 3673.

(79) Gould, I. R.; Moody, R.; Farid, S. *J. Am. Chem. Soc.* **1988**, *110*, 7242.

(80) Liang, N.; Miller, J. R.; Closs, G. L. *J. Am. Chem. Soc.* **1990**, *112*, 5353.

(81) k_f and k_r are calculated using equivalent parameters but opposite signs of the free energy. Our attempts to calculate reversibility with eq 11 were unsuccessful based on $\Delta G^\circ = -k_b T \ln(k_f/k_r)$ and calculation of the forward and reverse rate constants. Eq 30 was shown to be reversible and was used in the calculation of k_{nr}.

(82) Damrauer, N. H.; Cerullo, G.; Yeh, A.; Boussie, T. R.; Shank, C. V.; McCusker, J. K. *Science* **1997**, *275*, 54.